Homopolar Magnetic Bearing Saturation Effects on Rotating Machinery Vibration

Kyungdae Kang[1] and Alan Palazzolo[2]

[1]Samsung Techwin Co., LTD, Seongnam-si, Gyeonggi-do 463-400, South Korea
[2]Mechanical Engineering, Texas A&M University, College Station, TX 77843 USA

An objective in the design of high performance machinery is to minimize weight so magnetic bearings are often designed to operate slightly lower than their magnetic material saturation. Further weight reduction in the bearings requires operation in the nonlinear portion of the B-H curve. This necessitates a more sophisticated analysis at the bearing and rotordynamic system levels during the design stage. This paper addresses this problem in a unique manner by developing a fully nonlinear homopolar magnetic bearing model. The nonlinear dynamics of a permanent magnet-biased homopolar magnetic bearing (PMB HoMB) system with a flexible rotor is analyzed. Nonlinear effects due to power amplifier voltage and current saturation and position dependent reluctances are also included in the model. A new curve fit model of the B-H curve is shown to have significantly better agreement with the measured counterpart than conventional piecewise linear. The modified Langmuir method, with a novel correction terms for the weak flux region, is used to form an analytical model of the experimental magnetization curve of Hiperco 50. High static and dynamic loads applied to the rotor force the magnetic bearing to operate in a flux saturated state. The response of the heavily loaded 4-DOF rotor-bearing system shows that limit cycle stability can be achieved due to the magnetic flux saturation or current saturation in the amplifier. The stable limit cycle prevents the linear model instability, creating what is experimentally observed as a "virtual catcher bearing." To the authors' knowledge this is the first explanation of this commonly observed phenomenon.

Index Terms—**Bearings (mechanical), vibrations.**

I. Introduction

In general, magnetic bearings are classified in two groups: heteropolar and homopolar. Heteropolar magnetic bearings (HeMB) designs employ magnetic fields that include both N and S poles around the circumference of the bearing, whereas homopolar magnetic bearings (HoMB) have either all N poles or all S poles. HoMB most often employ permanent magnets to provide the DC bias field. The improvement of efficiency which this provides, and the reduction of eddy currents that result from eliminating complete flux reversals are distinct advantages of HoMB over HeMB. Extensive research has been done in nonlinear dynamics analysis of rotor-active magnetic bearing (AMB) systems, but there are few publications dealing with the effect of magnetic saturation and amplifier voltage/current saturation on the nonlinear dynamic response of rotor. This is especially true for HoMB designs. Maslen *et al.* investigated the performance limits of HeMB, such as peak force, slew rate, and displacement sensitivity [1]. He found that peak force limitation is primarily due to the nonlinearity in the magnetization curve of the electromagnet core material and force slew rate limit is caused by the power amplifier voltage limit, which results in phase lag and reduction in both stiffness and damping in the bearing. For PMB HoMB, Lee *et al.* studied similar performance limits [2], however these two papers do not deal with the effects of saturation on nonlinear dynamic response of a flexible rotor. They instead focus solely on the effect of magnetic core saturation on the maximum static force, and on the power amplifier voltage saturation's effect on the force slew rate. Chinta investigated the forced response of a two-dof (x-y) rigid rotor supported symmetrically by identical heteropolar magnetic bearings, including imbalance excitation, and a simple bilinear model of magnetic flux saturation [3], [4]. Flux saturation was found to reduce the maximum forces depending on the rotor speed. Steinschaden *et al.* investigated the dynamics of an active magnetic bearing system for the case of large rotor eccentricities [5]. They modeled the nonlinearities such as magnetic saturation effect, saturation of the amplifier and of the control current, but only present results from the control current limit. These authors restrict application of their approach to light saturation where their bilinear B-H type model is most suitable and not for the case of heavy saturation, above the starting point of the second linear part of the bilinear B-H curve. For specific parameter sets, symmetry breaking and quasiperiodic solution result from the effects of current saturation.

Analytical (curve fit) models of the magnetization curve have been formed in various way, such as an exponential series [6], rational-fraction approximations [7], [8], and modified exponential functions [9]. These approximations are suitable for the magnetization curves with low initial slope, and do not fit to the weak flux region very well.

We propose a modified Langmuir method with the correction terms for the weak flux region to form an analytical model of the experimental magnetization curve of Hiperco 50. This improves the prediction of the magnetic force when the bearing is operating dynamically with both weak and high magnetic fluxes. This approach is employed for the nonlinear analysis of a heavily loaded 4-degree-of-freedom (DOF) flexible rotor-bearing system. Heavy static and dynamic loads applied to the rotor causes the magnetic bearings to operate within the regions of the magnetic bearing clearance that cause

Manuscript received June 18, 2011; revised October 27, 2011; accepted December 07, 2011. Date of publication January 05, 2012; date of current version May 18, 2012. Corresponding author: A. Palazzolo (e-mail: a-palazzolo@tamu.edu).

Color versions of one or more of the figures in this paper are available online at http://ieeexplore.ieee.org.

Digital Object Identifier 10.1109/TMAG.2012.2182776

flux saturation. The response of the system shows that limit cycle stability can be achieved due to the magnetic flux saturation or current saturation in the amplifier; otherwise the system would experience a destructive instability. This simulation results provide the first explanation of this commonly observed limit cycle which is referred to as a "virtual catcher bearings." Analysis of nonlinear dynamics of the flexible rotor operation in the magnetic flux saturation zone may make it practical to utilize the full load capacity of the magnetic bearings by predicting the rotor response for large motions or with heavy static loads.

II. Analytical Magnetization Curve for Magnetic Circuit Equations

Previous models [6]–[10] of the magnetization curve develop an equation for B as a function of H, however solution of a magnetic circuit model for flux requires a material description in the form of H as a function of B, which follows from Ampere's law stated in terms of H. This approach easily permits the system of coupled magnetic circuit equations to be expressed in terms of a set of fluxes, which are made independent by applying conservation of flux. This is illustrated in the following analysis of a homopolar magnetic bearing with permanent magnet bias and material saturation effects.

The proposed function is a modified Langmuir method with a polynomial function multiplied by probability density type function, which acts as a correction term for the weak flux region. The analytical approximation of the experimental magnetization curve of Hiperco 50 becomes

$$H = \frac{P}{(1+Q\cdot B^R)^2} - P + \frac{1}{\sqrt{2\pi\sigma^2}} e^{\frac{-B^2}{2\sigma^2}} \cdot(a_0 + a_1 B + a_2 B^2 + a_3 B^3 + a_4 B^4 + a_5 B^5 + a_6 B^6) \quad (1)$$

where H is the magnetic field intensity (A·turn/m); B is the magnetic flux density (Tesla) $(0 \le \mathrm{B} \le 2.4)$; P, Q, R, σ, and $\mathrm{a_0} \sim \mathrm{a_6}$ are the constants. Fig. 1 shows the comparison plot between the curve of the analytical model from (1) fitted to the experimental data found in NASA technical report [11] and the bilinear model fit from (2) that is published in [5].

$$\mu_{r,mi} = \frac{1-\mu_{r,mi,0}}{\pi} \times \arctan\left(K_{M,mi}\frac{|B_{mi}| - B_{mi,\max}}{B_{mi,\max}}\right) + \frac{1+\mu_{r,mi,0}}{2} \quad (2)$$

The bilinear B-H curve model shown in (2) provides the effective relative permeability values, where $\mu_{r,mi,0}$ is the relative permeability well below the saturation value $B_{mi,\max}$, B_{mi} is the actual magnetic flux density, $K_{M,mi}$ is a shaping factor of the B-H curve, and i denotes the number of poles $(\mathrm{i} = 1,\ldots,6)$. The parameter values utilized in (2) are values provided in the reference: $B_{mi,\max} = 2.0$, and $K_{M,mi} = 100$ and $\mu_{r,mi,0} = 8000$ was chosen, based on the line that passes through the second and fifth data points.

The constants in (1) can be determined by minimizing the appropriate cost function. The relative deviation [10] of the magnetic intensity $H(B_i)$ calculated by (1) from the experimental values H_i appears in the cost function as

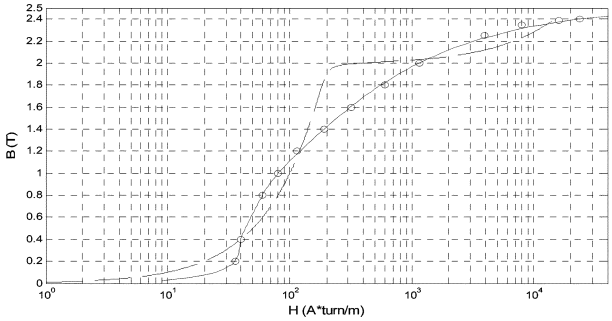

Fig. 1. Curve fits of Hiperco 50 experimental B-H curve. Key: o, Hiperco 50 experimental data; —, proposed model; − −, bilinear model.

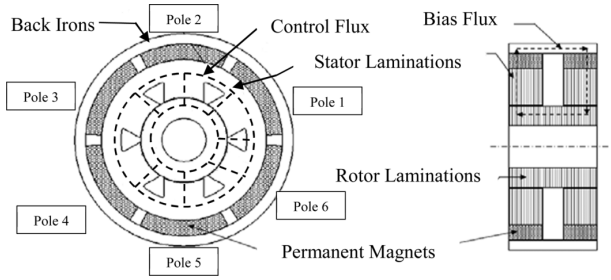

Fig. 2. Dual active plane, permanent magnet-biased homopolar magnetic bearing.

$$D_i = \sqrt{\left|\frac{H(B_i) - H_i}{H(B_i) + H_i}\right|}. \quad (3)$$

The cost function has the form

$$F_{\text{cost}} = \sum_{i=1}^{n} h_i D_i \quad (4)$$

where $\mathrm{h_i}$ is a weighting factor for $\mathrm{i} = 1,\ldots,\mathrm{n}$, where n is the number of experimental data points. The constants in (1) are determined as

$$\begin{aligned} &P = 0.9943, \quad Q = -0.8905, \quad R = 0.1242 \\ &\sigma = 2.1746\times10^{-1}, \quad a_0 = 1.2239\times10^{-3}, \\ &a_1 = -5.7293, \\ &a_2 = 2.1655\times10^{3}, \quad a_3 = -1.5777\times10^{4}, \\ &a_4 = 5.1068\times10^{4}, \\ &a_5 = -7.8144\times10^{4}, a_6 = 5.0641\times10^{4}. \end{aligned}$$

III. Rotor-Bearing System Model

A. Magnetic Circuit Model

Reference [12] provides a good overview of the PMB HoMB components, configuration and design approach for fault tolerant operation. This discussion is expanded in [13] for ultra-

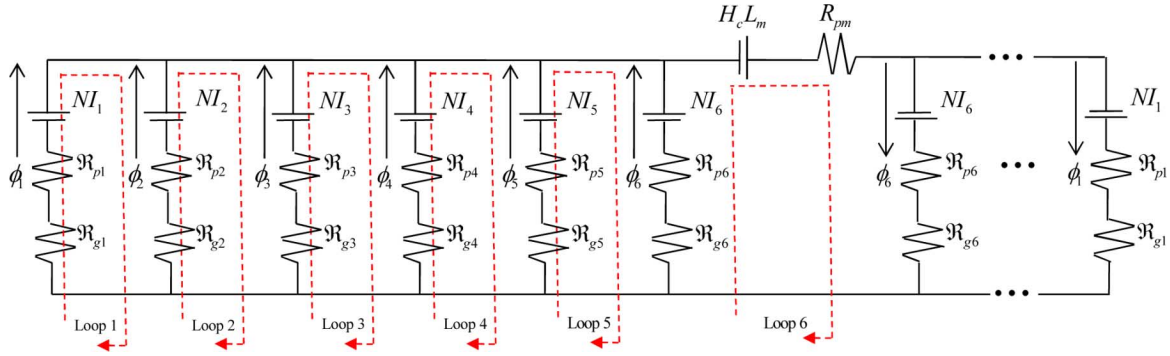

Fig. 3. 1-D magnetic circuit model of homopolar magnetic bearing with permanent magnet and electric coil sources.

high temperature applications. For illustration purposes consider a six-pole PMB HoMB consisting of two stator lamination packs, 12 permanent magnets, electric coils on each pole, and back irons. Six permanent magnets are placed circumferentially on each stator lamination pack as shown in Fig. 2. The permanent magnets provide the magnetic bias flux which flows both axially and radially and is commonly used to provide the reaction force to counter the static load applied to the bearing. The control flux is produced by the electric coils and is restricted to radial and circumferential flow in the rotor and stator lamination stacks. This flux component is used to regulate the shaft position at the target location within the magnetic bearing clearance circle (gap), and to produce desired stiffness, damping and disturbance cancellation forces.

Fig. 3 shows the magnetic circuit model including 6 independent fluxes, 6 gap and 6 pole reluctances, 6 NI current sources and a lumped permanent magnet source along with its reluctance. The right hand side plane in Fig. 3 has an identical magnetic circuit as the left hand side and operates symmetrically with identical sources, parameter values and fluxes. Hence the right hand side is only partially shown in Fig. 3. The magnetic circuit is a highly simplified, yet reasonably accurate representation of the actual 3 dimensional magnetic field that actually occurs in the real system. The circuit fluxes are typically reduced by a de-rate factor (typically 0.75–0.9) to account for fringing at air gaps and leakage around air gaps. For the sake of illustration, the model presented here utilizes unity de-rate factors and concentrates the material paths in the pole reluctance terms.

Loops 1 to 5 represent radial flux paths, with each loop containing two poles, gap reluctances and magnetomotive forces for an adjacent set of poles. The pole reluctances represent the general causal relation between source and flux including the nonlinear B-H expression in (1) which incorporates flux saturation into the model. The pole reluctances increase with saturation since they are inversely proportional to the slope of the B-H curve in Fig. 1. The axial flux path is expressed in loop 6 which contains the permanent magnet source and reluctance terms. For the sake of illustration, only the pole material is assumed to be saturated.

Ampere's law is expressed for the present application by (5) and is used to generate a single equation for each loop. The air gap reluctances are linear in their source—flux causal relation and are dependent on the instantaneous air gaps determined by radial motions of the journal. This dependence and the Maxwell stress tensor force formula's dependence on the square of flux, causes the magnetic bearing forces to become nonlinear functions of the displacement coordinates at the bearings. This holds even in the absence of saturation in the material or in the feedback components.

The $\mathrm{H_{pi}}$-$\mathrm{B_{pi}}$ relation in (1) is substituted into the Ampere's law (5) to obtain 6 nonlinear algebraic equations for the 6 unknown fluxes, ϕ_i. The magnetic bearing control currents and x and y gaps, in the air gap reluctance terms, change continuously when the magnetic bearing is operating. Therefore, in general (6) must be solved for the fluxes at each integration time step in the simulation of the entire rotor-bearing system.

$$\oint H(\phi)\cdot dl = NI \tag{5}$$

$$\begin{aligned}
&\text{Loop 1}: \quad (H_{p1}-H_{p2})L_p + H_{g1}L_{g1} - H_{g2}L_{g2} \\
&\quad = N(I_1 - I_2) \\
&\text{Loop 2}: \quad (H_{p2}-H_{p3})L_p + H_{g2}L_{g2} - H_{g3}L_{g3} \\
&\quad = N(I_2 - I_3) \\
&\text{Loop 3}: \quad (H_{p3}-H_{p4})L_p + H_{g3}L_{g3} - H_{g4}L_{g4} \\
&\quad = N(I_3 - I_4) \\
&\text{Loop 4}: \quad (H_{p4}-H_{p5})L_p + H_{g4}L_{g4} - H_{g5}L_{g5} \\
&\quad = N(I_4 - I_5) \\
&\text{Loop 5}: \quad (H_{p5}-H_{p6})L_p + H_{g5}L_{g5} - H_{g6}L_{g6} \\
&\quad = N(I_5 - I_6) \\
&\text{Loop 6}: \quad H_{p6}L_p + H_{g6}L_{g6} + H_{\mathrm{pm}}L_m \\
&\quad = NI_6 + H_c L_m
\end{aligned} \tag{6}$$

where

$$\begin{aligned}
H_{pi} &= \frac{P}{\left(1+Q\cdot {B_{pi}}^R\right)^2} - P + \frac{1}{\sqrt{2\pi\sigma^2}} e^{-\frac{B_{pi}^2}{2\sigma^2}} \\
&\quad \cdot \left(a_0 + a_1 B_{pi} + a_2 {B_{pi}}^2 + a_3 {B_{pi}}^3 \right. \\
&\quad \left. + a_4 B_{pi}^4 + a_5 B_{pi}^5 + a_6 B_{pi}^6\right); \\
B_{pi} &= \frac{\phi_i}{A_p}; \quad H_{gi} = \frac{\phi_i}{\mu_0 A_g}; \quad H_{pm} = \frac{\phi_i}{\mu_{pm} A_m};
\end{aligned}$$

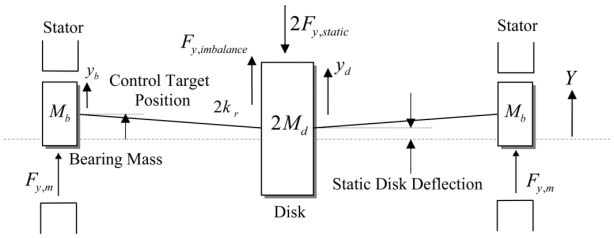

Fig. 4. Flexible shaft model with 4-DOF and Y direction static loading.

μ_0	permeability of free space;
$\mu_{\rm pm}$	permeability of the permanent magnet;
$\rm H_c$	coercivity of the permanent magnet;
$\rm L_p$	length of the pole; $\rm A_p$: pole area;
$\rm L_{gi}$	instantaneous length of the ith air gap; $\rm A_g$: air gap area
$\rm L_m$	length of the permanent magnet; $\rm A_m$: permanent magnet area;
N	number of coil turns per pole;
$\rm I_i$	current applied to the ith pole, $\rm i = 1$ to 6.

B. Flexible Rotor Model With Static Force

The rotor is modeled with two, radial PMB HoMBs. A magnetic thrust bearing is used for axial position control, but is not included in the present model since it is typically the case that the radial and axial magnetic bearings are uncoupled.

Fig. 4 shows the 4-DOF flexible rotor model including the bearings, central disk and bearing lumped masses, static and imbalance loads, and bearing and disc coordinates. The model neglects gyroscopic effects, and the resulting equations of motion with imbalance force and static force in the negative y direction are shown in (7). The shaft model is simplified relative to those of actual compressors, turbines, etc., in order to focus on the high fidelity, nonlinear magnetic bearing model and to make the system model more amenable to numerical integration based simulation. This "translation only" model is commonly used in the rotordynamics literature and is referred to as a "Jeffcott" rotor model. The disk in Fig. 4 is centrally (symmetrically) located between the identical bearings which is consistent with the use of a 1/2 rotor model. The imbalance is attached to this disk so as to not excite tilt or unsymmetric modes. The target positions for the journals in the magnetic bearings are intentionally set above the centers of the magnetic bearing clearance circles in order for the static load to be balanced by the permanent magnet bias flux. This commonly employed approach yields a significant reduction in coil currents and in the resulting ohmic losses.

$$\begin{aligned} M_b\ddot{x}_b + k_r(x_b - x_d) &= F_{x,m} \\ M_d\ddot{x}_d + k_r(x_d - x_b) &= M_d e\omega^2\cos(\omega t) \\ M_b\ddot{y}_b + k_r(y_b - y_d) &= F_{y,m} \\ M_d\ddot{y}_d + k_r(y_d - y_b) &= M_d e\omega^2\sin(\omega t) - F_{y,\rm static} \end{aligned} \quad (7)$$

where

M_b	concentrated mass lumped at the bearing;
$2M_d$	concentrated mass lumped at the central disc;
$2k_r$	effective shaft stiffness connecting the bearings and the disk;
ω	shaft spin rate in rad/s;
e	eccentricity of disk mass center;
$2F_{y,\rm static}$	static load applied to central disk;
$F_{x,m}, F_{y,m}$	magnetic bearing x and y forces.

C. System Control Loop

Each magnetic bearing has 2 parallel stator and rotor stacks of laminations that are offset axially, and are sometimes referred to as "active planes." Axially adjacent poles in these stacks have identical coils, are wired in series and are powered by the same power amplifier. This approach facilitates fault tolerant operation (FTO) of the magnetic bearings as explained in [12]. Implementation of FTO requires use of a "decoupling choke" to electrically stabilize the magnetic bearing by converting a singular inductance matrix into a diagonal matrix with zero mutual inductances between the poles. This approach for FTO was first proposed in [14] for HeMB. The model used here has fully operational coils since FTO is not of primary importance in this study. The 6 power amplifiers in Fig. 5 drive currents through the 6 pole/coil pairs to produce x and y radial control forces at each bearing. The controller is composed of a proportional-derivative (PD) stage, lag compensation (LC) and a low-pass filter (LPF) to represent input and output filters on a digital controller. This model is again simplified to focus primarily on the nonlinear aspects of the model, while utilizing credible components in other areas. Inclusion of the LC, LPF and power amplifier (PA) dynamics in the model accounts for the loss in phase margin that destabilizes real magnetic bearing systems. The LC is employed as a pseudo-finite gain integrator to reduce the static offset error (droop) caused by the static loading. Transfer functions for the LC, LPF, and PA are described in (8), (9), and (10), respectively.

$$D_{\rm LC}(s) = \frac{s+z}{s+p}, \quad z > p \quad (8)$$

$$D_{\rm LPF}(s) = \frac{1}{(\tau s+1)^2}, \quad \tau = \frac{1}{2\pi f_c}, \quad f_c : \text{cutoff frequency} \quad (9)$$

$$D_{\rm PA}(s) = \frac{1}{Ls+R}, \quad L : \text{coil inductance}, \quad R : \text{coil resistance}. \quad (10)$$

The X and Y control voltages are routed into a current distribution matrix (CDM) [12] which outputs linear combinations of the input voltages to the 6 power amplifiers (PAs) which drive currents through the 6 pole/coil pairs. Any of the PA voltages or currents may saturate as indicated by Fig. 6, where $V_{\rm CDMi}$ is the

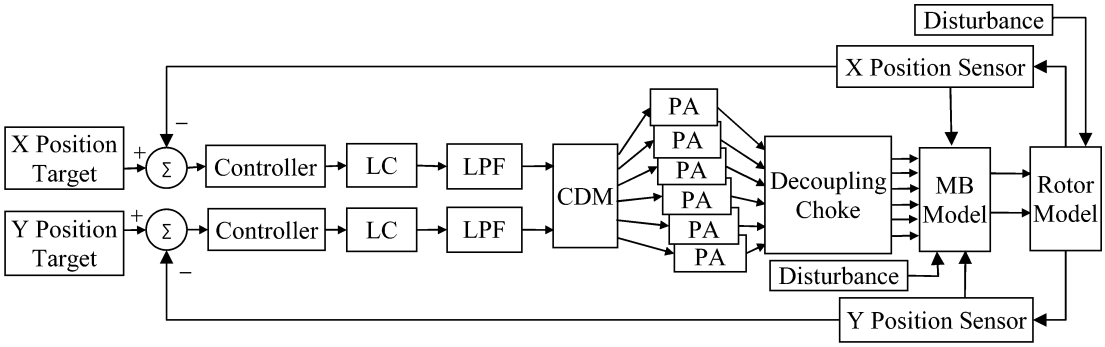

Fig. 5. Diagram for journal motions feedback position control.

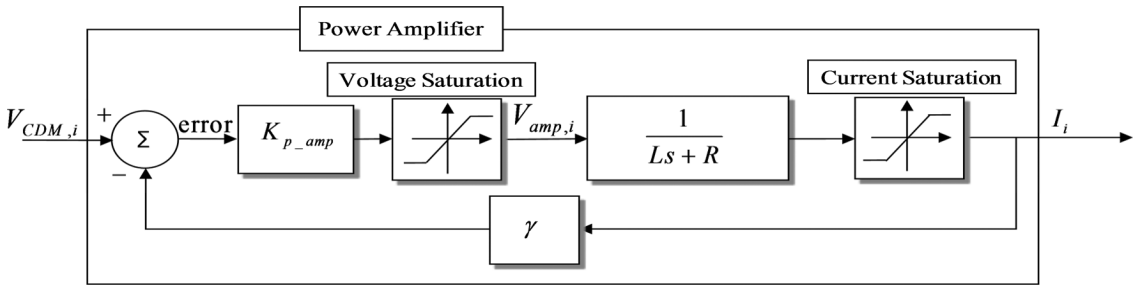

Fig. 6. Simplified power amplifier model with output voltage and current saturation limiters.

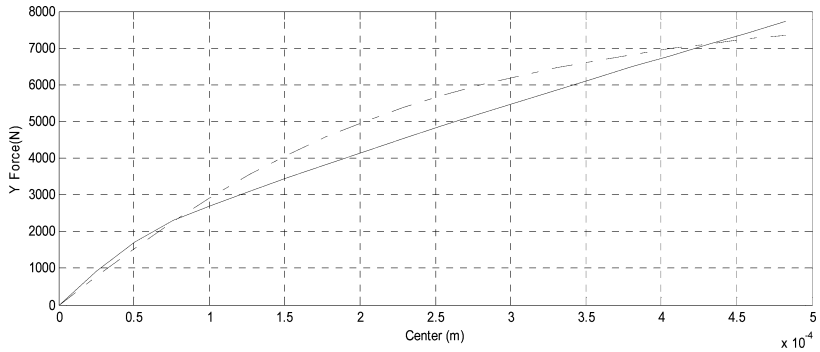

Fig. 7. Y force vs. Y journal position with bilinear and proposed saturation models. Key: —, bilinear; – · –, proposed.

voltage output from the CDM, and V_{ampi} is the voltage output and I_i is the current output from PA $(\mathrm{i} = 1, \ldots, 6)$.

The PMB HoMB magnetic circuit model of (6) provides a means to calculate the 6 fluxes shown in Fig. 3 given the instantaneous 6 currents I_i, and the X and Y journal coordinates. The Levenberg-Marquardt algorithm [15] is used to solve the set of nonlinear algebraic equations, (6), given the solution for the fluxes from the previous time step are used as initial guesses of their values for the present step.

Fluxes from (6) are utilized in (11) to determine the X and Y forces. The forces are modified by the derate factors χ_i to correct the 1-D magnetic circuit model for 2-D and 3-D effects, including fringing and leakage. The derate factors are typically selected in the range 0.7–0.9, although for the sake of illustration the results here are shown for $\chi_i = 1$

$$F_i = \frac{\chi_i \phi_i^2}{2\mu_0 A_g}, \quad i = 1, \ldots, 6$$

$$F_{x,m} = \sum_{i=1}^{6} F_i \cos(\theta_i) \quad F_{y,m} = \sum_{i=1}^{6} F_i \sin(\theta_i). \quad (11)$$

IV. Results and Discussion

A. Bilinear and Modified Langmuir Saturation Models

Fig. 7 shows the Y direction force vs. Y direction journal position, from the magnetic circuit model with the proposed B-H curve and the bilinear type B-H curve models from (2), and with the parameter values from Section II. The currents are zero so the flux is driven only with the permanent magnets. The coercive field intensity $(\mathrm{H_c})$ of the permanent magnets is 633 kA/m and the residual flux density $(\mathrm{B_r})$ is 0.855 T at room temperature. The air gap length in the PMB HoMB is 5.080×10^{-4} m.

From Fig. 7, the forces generated when the bilinear type$B$-H curve model is used are smaller than those with the proposed B-H curve model beyond 7.6×10^{-5} m in the Y direction. The proposed B-H curve model closely follows the experimental data, thus the bilinear B-H curve model is less suitable for rotor motion simulations. Fig. 8 shows the flux density in each pole vs. Y journal position utilizing the proposed and bilinear B-H curve models. Fig. 7 shows predicted force differences as large as 15% between the the modified Langmuir and bilinear based

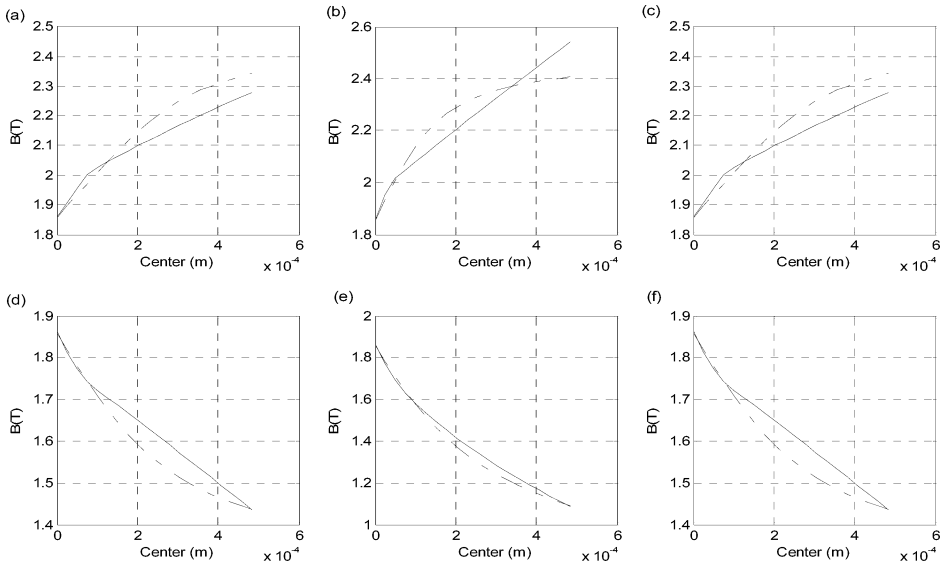

Fig. 8. Flux density in each pole vs. Y journal position. Key: —, bilinear; − − −, proposed; (a) pole 1, (b) pole 2, (c) pole 3, (d) pole 4, (e) pole 5, and (f) pole 6.

TABLE I
PARAMETER SETS FOR SATURATION EFFECTS EXAMPLE

Case		PA Dynamics	Voltage Saturation	Current Saturation	Magnetic Flux Saturation	LPF, PA cutoff (Hz)	Static force (N, N mm^{-2})	G_p , G_d
1		N	N	N	N	1900, N.A.	3903.8, 1.33	75.17, 0.0158
	2.1	Y	N	N	N	4000, 1000	3903.8, 1.33	75.17, 0.0423
2	2.2	Y	Y	N	N	4000, 1000	3903.8, 1.33	75.17, 0.0423
	2.3	Y	N	Y	N	4000, 1000	3903.8, 1.33	75.17, 0.0423
3		N	N	N	Y	1900, N.A.	2939.6, 1.00	75.17, 0.0158
4		Y	Y	Y	Y	6000, 1000	2939.6, 1.00	75.17, 0.0423

curve fit models. Likewise, Fig. 8 shows differences in flux density up to 6%.

B. Flexible Shaft Model With Heavily Loaded Bearings

This section illustrates the effects of flux and power amplifier current and voltage saturations on the nonlinear dynamic response of the flexible shaft model subjected to heavy static and dynamic loading. This is representative of a high load to weight ratio bearing with light to blade-out levels of imbalance. Figs. 4 and 5 show the 4-DOF flexible shaft and feedback control models. The parameters for the cases considered are shown in Table I.

The target (reference) point is offset from the centered position in the opposite static load direction by an amount of 1.02×10^{-4} m in order to reduce the demand for electric current by employing the permanent magnet flux force to counteract the static load. Proportional gain $(\mathrm{G_P})$ and derivative gain $(\mathrm{G_d})$ of the controller are the same in the x and y directions and the effective shaft stiffness $(\mathrm{k_r})$ is 4.7×10^7 N/m. The pole path length is 3.81×10^{-2} m, the masses at the disk $(\mathrm{M_d})$ and bearing $(\mathrm{M_b})$ are 17.11 kg and 3.421 kg, respectively. The low-pass filter (LPF) stage is typically included to suppress electrical noise, shaft runout or for anti-aliasing. Note the case 1 value 1900 Hz of LPF cutoff frequency causes an unstable response for the model configuration that omits amplifier dynamics and flux saturation. This is illustrated in Fig. 9 which shows the X and Y displacements at the disk and bearing locations. The instability frequency 990 Hz in Fig. 13 indicates that the 2nd (shaft bending) mode is unstable which is consistent with the loss of phase margin caused by the power amplifier and LPF. In reality these motions would cause impacts with the system's catcher bearings which are outside of the area of interest of the present work. The response remains unstable in case 2.1 where unsaturated amplifier dynamics are included in the model, as shown in Fig. 10. Cases 1 and 2.1 involve linear models to provide a comparison with the nonlinear model cases that include the effects of magnetic flux saturation and amplifier voltage/current saturation. The results in Figs. 9 and 10 clearly predict a very destructive, high amplitude and frequency vibration. In practice, a limit cycle will often form and arrest this linear model instability as demonstrated below.

Case 2.2 in Table I is identical to case 2.1 however the power amplifier voltage saturation is included with limiting voltages of ± 80 volts, and the current and flux saturation is excluded from the model. Fig. 11 shows that a limit cycle does not result from including voltage saturation and the system diverges in instability. Case 2.3 including power amplifier current saturation (limiting) at a value of ± 11 amps, while excluding both

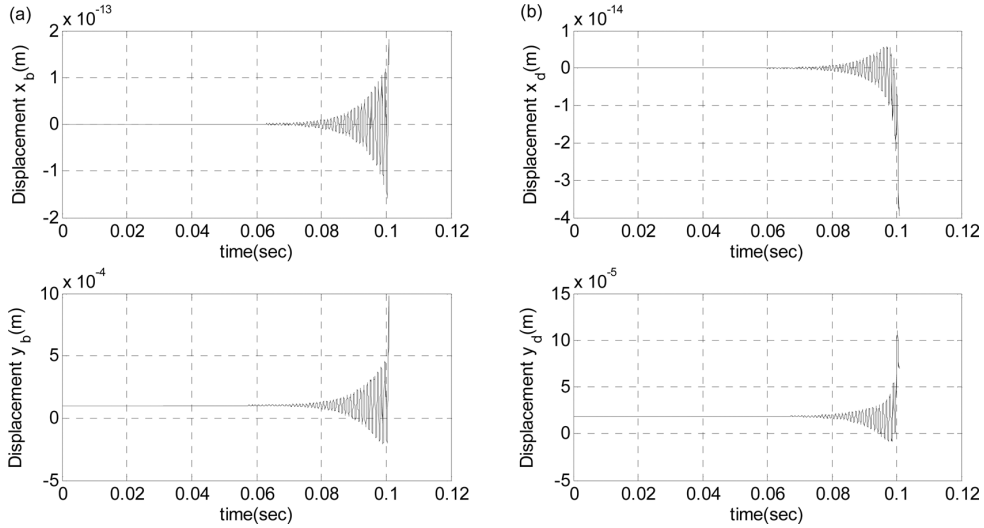

Fig. 9. X and Y initial responses at the (a) bearing and (b) rotor locations, excluding flux saturation, power amplifier saturation and power amplifier dynamics effects (Case 1).

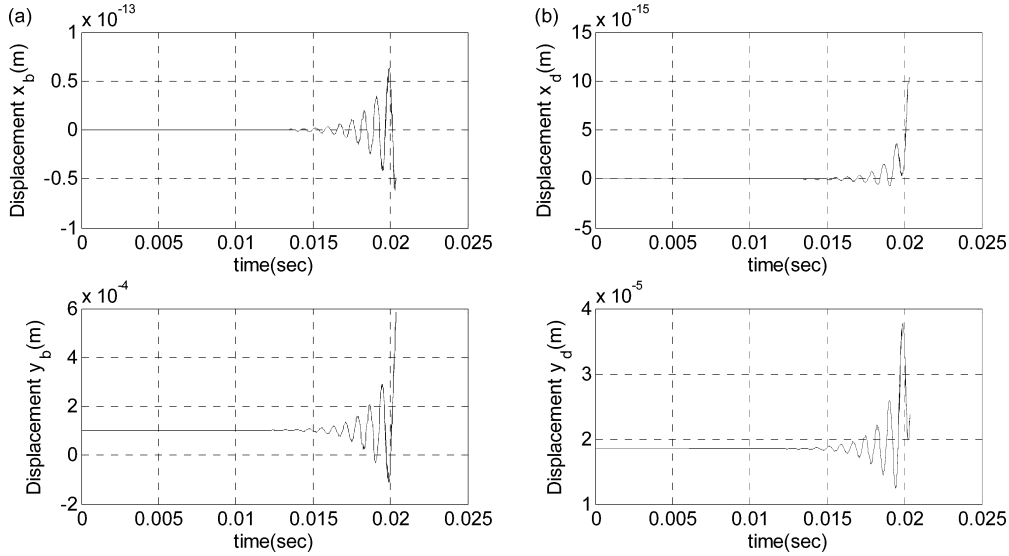

Fig. 10. X and Y initial responses at the (a) bearing and (b) rotor, excluding flux saturation and power amplifier saturation and including power amplifier dynamic effects (Case 2.1).

voltage and flux saturation, results in a stable, limit cycle response as shown in Fig. 12. The results in Figs. 11 and 12 indicate that the linear model instability is arrested in a nonlinear limit cycle when the effect of power amplifier current saturation is included in the model. This limit cycle is often observed in practice and is sometimes referred to as a "virtual catcher bearing".

The case 3 model includes material path flux saturation but excludes current and voltage saturation (limiting) effects in the power amplifiers. The air gap fluxes are weakened from the material path flux saturation leading to a loss of load capacity for counteracting the applied static load with the permanent magnet bias flux. The target (reference) position could be adjusted to compensate for this or the static load could be decreased to maintain the same target position in the Y direction. The latter approach was employed with a reduction of static applied load from a value of 3903.8 N to a value of 2939.6 N. Fig. 13 shows that the vibration becomes confined to a limit cycle similar with a Van der Pol type system, when magnetic flux saturation is included in the model. The response magnitude is within the clearance of 5.080×10^{-4} m. This phenomenon of a limit cycle preventing destructive unstable motion has been observed by the authors experimentally, and is caused by either current or flux saturations from Figs. 12 and 13, respectively.

The case 4 model that includes amplifier dynamics and flux saturation shows stable unbalance response when the LPF cutoff frequency is set to 6000 Hz. Note that the response oscillates about the target position and only has a synchronous response. This is illustrated at Fig. 14 when the journal rotates at 10000 rpm with the eccentricity of 3.81×10^{-5} m and the journal orbital response at the bearing is within the half of the bearing clearance, $\pm 2.54 \times 10^{-4}$ m. Stable operation results even with the top 3 pole flux densities exceeding saturation (2 T), as shown in Fig. 15. Thus the results in Fig. 15 helps dispel the notion that any material flux saturation is catastrophic for magnetic bearing control.

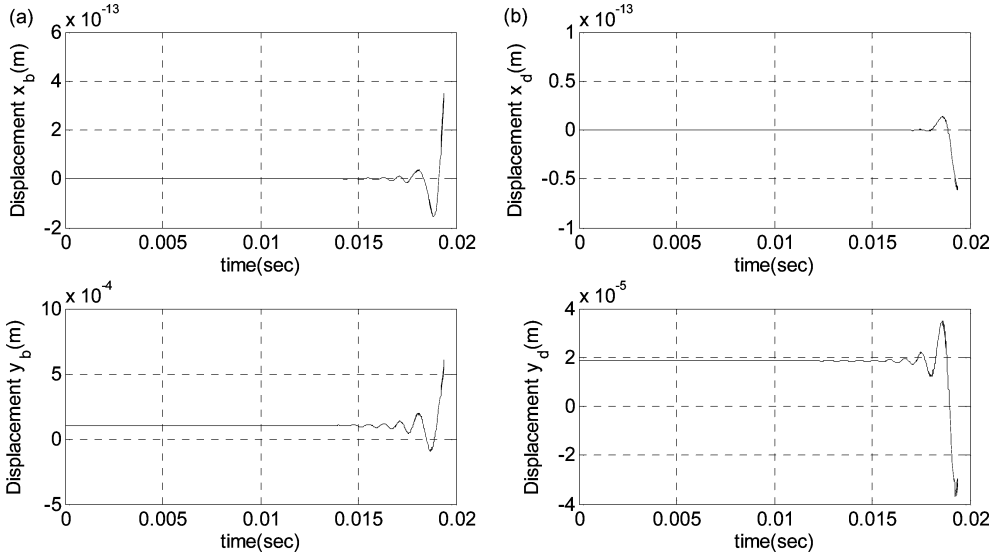

Fig. 11. X and Y initial responses at the (a) bearing and (b) rotor, excluding flux saturation and including power amplifier dynamics and voltage saturation (Case 2.2).

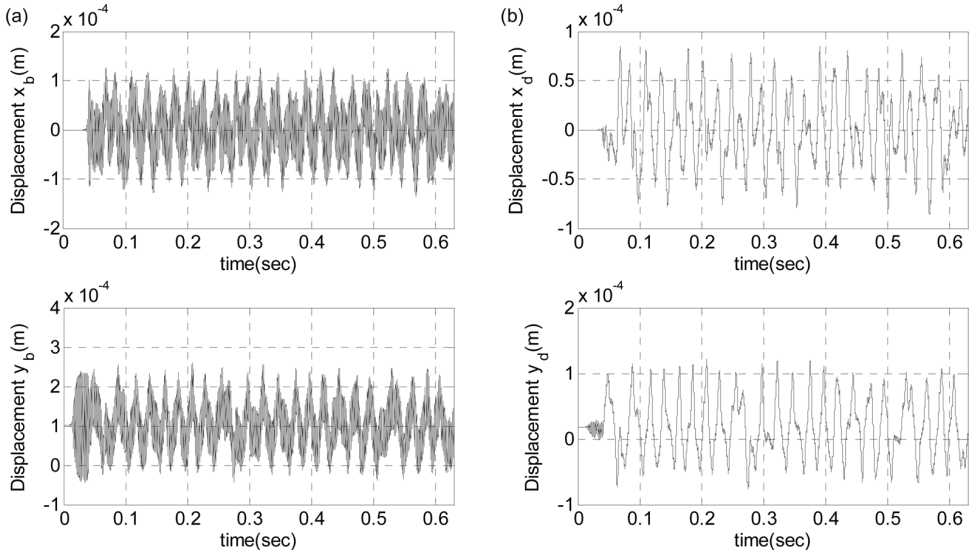

Fig. 12. X and Y initial responses at the (a) bearing and (b) rotor, excluding flux saturation and including power amplifier dynamics and current saturation (Case 2.3).

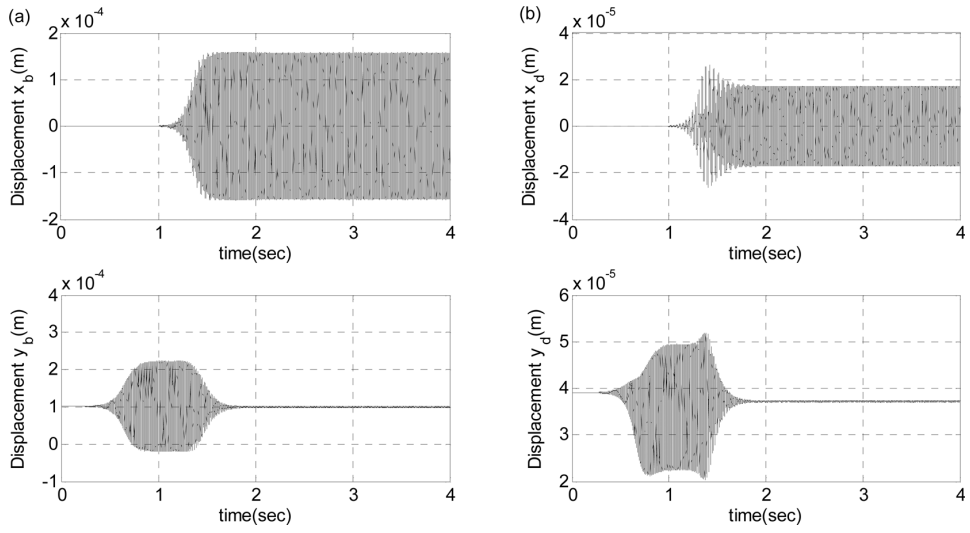

Fig. 13. X and Y initial responses at the (a) bearing and at (b) rotor, excluding power amplifier dynamics and saturation and including flux saturation (Case 3).

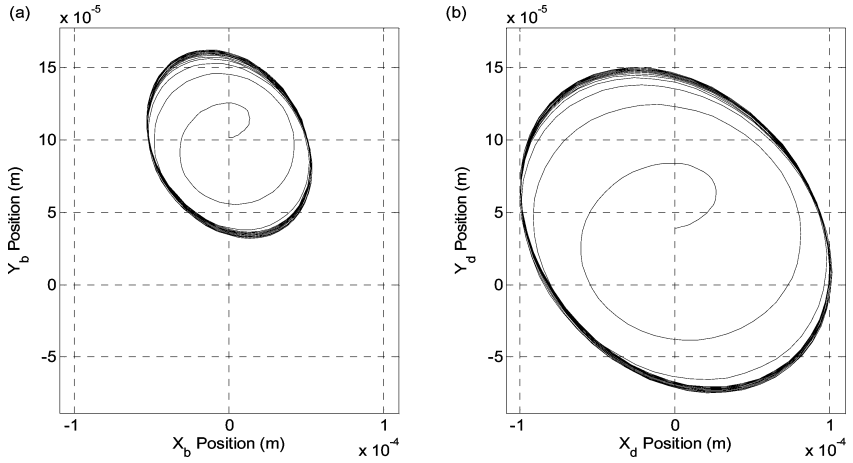

Fig. 14. Orbit plot of stable response at the (a) bearing and (b) disk with the model that includes amplifier dynamics and flux saturation, when the journal rotates at 10000 rpm with the eccentricity of 3.81×10^{-5} m (Case 4).

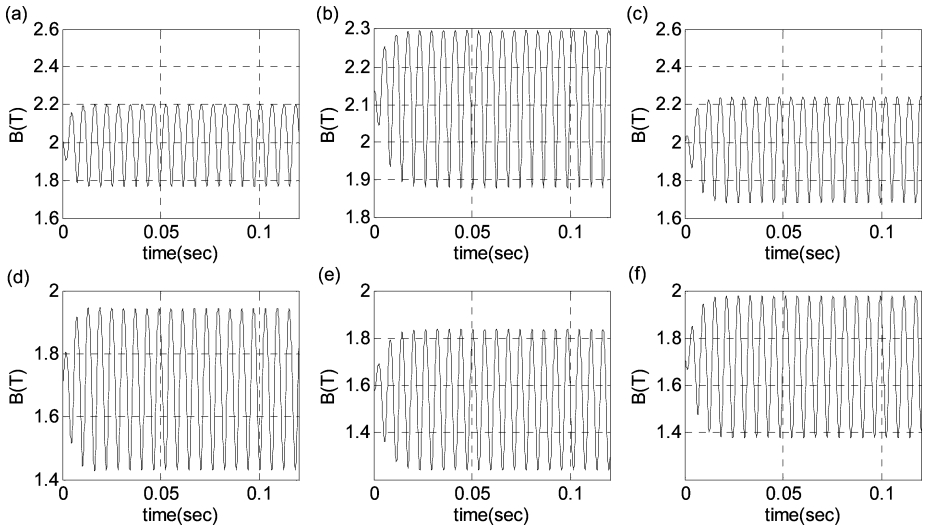

Fig. 15. Flux density in each pole with the model that includes amplifier dynamics and flux saturation, when the journal rotates at 10000 rpm with the eccentricity of 3.81×10^{-5} m. (a) pole 1, (b) pole 2, (c) pole 3, (d) pole 4, (e) pole 5, and (f) pole 6 (Case 4).

C. Static Load Capacity of the PMB HoMB With Flux Saturation

The maximum static load capacity of a PMB HoMB including saturation effects, was investigated through numerically integrated solutions. The externally applied static force may increase to the point that the PMB HoMB force become inadequate to balance it. As expected the static deflection gets smaller with increase in the proportional gain or lag compensator pole/zero value as shown in Fig. 16. The fluxes and currents in the individual poles are fairly insensitive to these same variables as shown in Figs. 17 and 18, respectively.

The benefits of moving the control target point away from the bearing center is clearly shown by considering Figs. 19 and 20. The actual steady state y position of the journal and control current in pole 2 are plotted vs. externally applied static loading for set points at the bearing center (0, 0) and (x,y) = (0, 2.032×10^{-4})m. The latter setpoint results in zero required current for

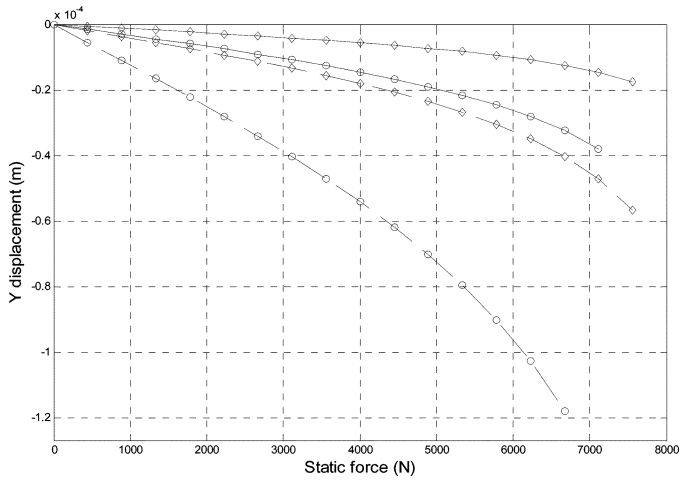

Fig. 16. Y Displacement vs. Static Force Key: $--$ o, z/p = 3 G_p = 39; $--$ $\diamond$, z/p = 3 G_p = 96;—o, z/p = 9 G_p = 39;—$\diamond$, z/p = 9 G_p = 96.

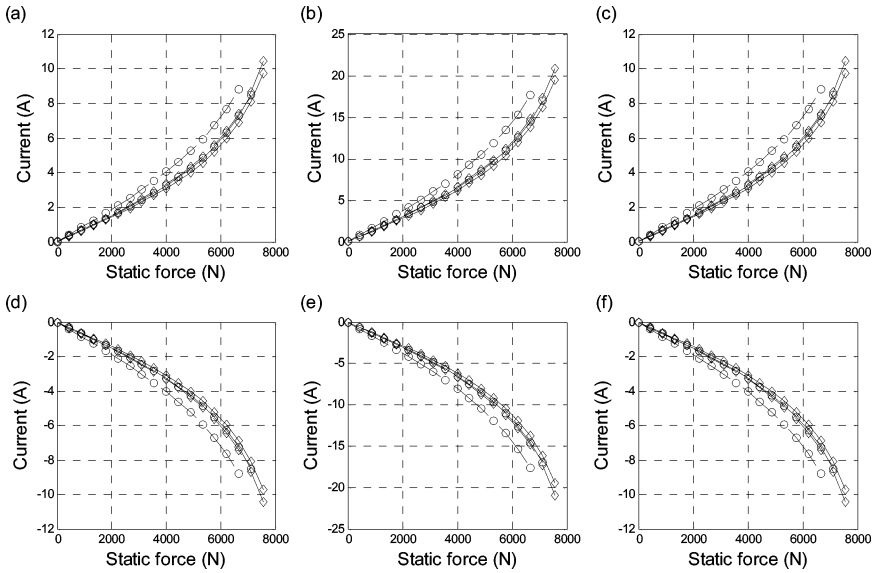

Fig. 17. Current vs. Static Force. Key: $--$ o, $z/p = 3$ $G_p = 39$; $--$ $\diamond$, $z/p = 3$ $G_p = 96$;—o, $z/p = 9$ $G_p = 39$;—$\diamond$, $z/p = 9$ $G_p = 96$ (a) pole 1, (b) pole 2, (c) pole 3, (d) pole 4, (e) pole 5, and (f) pole 6.

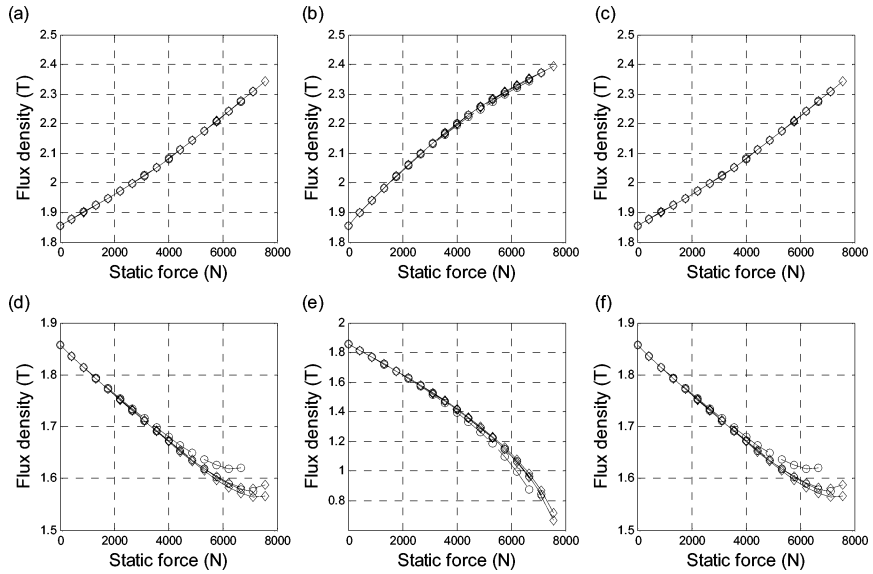

Fig. 18. Flux Density vs. Static Force. Key: $--$ o, $z/p = 3$ $G_p = 39$; $--$ $\diamond$, $z/p = 3$ $G_p = 96$;—o, $z/p = 9$ $G_p = 39$;—$\diamond$, $z/p = 9$ $G_p = 96$ (a) pole 1, (b) pole 2, (c) pole 3, (d) pole 4, (e) pole 5, and (f) pole 6.

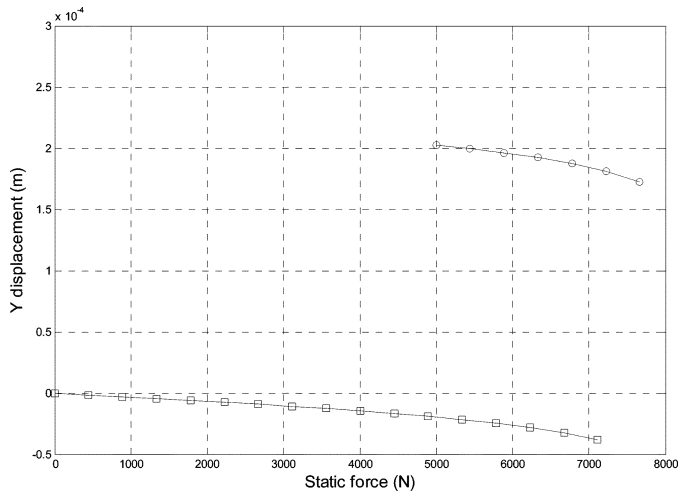

Fig. 19. Static force vs. Y displacement. $z/p = 9$, $G_p = 40$. Key: □, control target $Y = 0$ m; o, control target $Y = 2.032 \times 10^{-4}$ m.

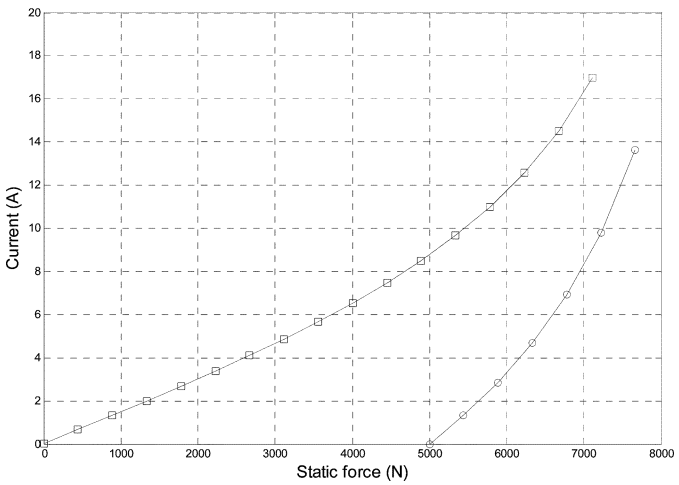

Fig. 20. Static force vs. current. $z/p = 9$, $G_p = 40$. Key: □, control target $Y = 0$ m; o, control target $Y = 2.032 \times 10^{-4}$ m.

an external load of 5 000 N, since the flux is generated entirely by the permanent magnets. Fig. 20 shows that utilizing the (0,0) setpoint instead of the shifted setpoint would result in a required current of 8 amps that could produce a significant i^2R ohmic loss.

As shown by Fig. 19, the flux densities in Fig. 18 correspond to stable levitation with flux density levels significantly exceeding the 2 Tesla linear limit. These result help dispel the notion that any material flux saturation is catastrophic for magnetic bearing control.

V. Conclusion and Future Work

The contributions of this paper include:

1) Introduction of a correction factor to the Langmuir B-H curve model that provides greater curve fit accuracy in the lower flux density range.
2) A systematic approach for the nonlinear modeling of a permanent magnet-biased homopolar magnetic bearing (PMB HoMB) utilizing the approach in (1) to express the magnetic field intensity H in terms of the flux density B
3) Demonstration of the ability of actuator flux or power amplifier current saturations to arrest linear system instability to form a limit cycle response, a phenomena that has been observed experimentally by the authors.
4) Simulation based demonstration for the stable control of a magnetic bearing supported, flexible shaft rotor with heavy flux saturation caused by high static and dynamic loading applied to the rotor.

Future work areas include consideration of the nonlinear effects of eddy currents [16], [17], and computationally efficient prediction of nonlinear steady state responses for large order rotor-magnetic bearing systems.

References

[1] E. H. Maslen, P. Hermann, M. Scott, and R. R. Humphris, "Practical limits to the performance of magnetic bearings: Peak force, slew rate, and displacement sensitivity," *J. Tribol.*, vol. 111, pp. 331–336, 1989.

[2] A.-C. Lee, F.-Z. Hsiao, and D. Ko, "Performance limits of permanent-magnet-biased magnetic bearings," *JSME Int. J.*, ser. C: Dynamics, Control, Robotics, Design and Manufacturing, vol. 37, pp. 783–794, 1994.

[3] M. Chinta and A. B. Palazzolo, "Stability and bifurcation of rotor motion in a magnetic bearing," *J. Sound Vib.*, vol. 214, pp. 793–803, 1998.

[4] M. Chinta, "Steady State Nonlinear Rotordynamics and Modeling of Magnetic Bearings," Ph.D. dissertation, Dept. Mech. Eng., Texas A&M Univ., College Station, TX, 1997, 138.

[5] N. Steinschaden, "Nonlinear stability analysis of active magnetic bearings," in *Fifth Int. Symp. Magnetic Suspension Technology*, 1999, pp. 411–427.

[6] W. K. Macfadyen, R. R. S. Simpson, R. D. Slater, and W. S. Wood, "Representation of magnetization curves by exponential series," *Proc. Inst. Elect. Eng.*, vol. 120, pp. 902–904, 1973.

[7] J. Rivas, J. M. Zamarro, E. Martin, and C. Pereira, "Simple approximation for magnetization curves and hysteresis loops," *IEEE Trans. Magn.*, vol. MAG-17, no. 4, pp. 1498–1502, Jul. 1981.

[8] G. F. T. Widger, "Representation of magnetisation curves over extensive range by rational-fraction approximations," *Proc. Inst. Elect. Eng.*, vol. 116, pp. 156–160, 1969.

[9] N. Shimatani and H. Fujita, "Approximation of magnetization curves by exponential functions," *Elect. Eng. Jpn. (English translation of Denki Gakkai Ronbunshi)*, vol. 101, pp. 1–10, 1981.

[10] Z. Wodarski, "Analytical description of magnetization curves," *Phys. B: Condens. Matter*, vol. 373, pp. 323–327, 2006.

[11] P. E. Kueser, D. M. Pavlovic, D. H. Lane, J. J. Clark, and M. Spewock, "Properties of Magnetic Materials for Use in High-Temperature Space Power Systems," NASA Tech. Rep., SP-3043, 1967.

[12] M.-H. Li, A. B. Palazzolo, A. Kenny, A. J. Provenza, R. F. Beach, and A. F. Kascak, "Fault-tolerant homopolar magnetic bearings," *IEEE Trans. Magn.*, vol. 40, no. 5, pp. 3308–3318, Sep. 2004.

[13] A. Palazzolo, R. Tucker, K.-D. Kang, A. Kenny, V. Ghandi, J. Liu, H. Choi, and A. Provenza, "High temperature, permanent magnet biased, fault tolerant, homopolar magnetic bearing development," in *ASME Turbo Expo*, Berlin, Germany, Jun. 9–13, 2008, pp. 1203–1214.

[14] E. H. Maslen and D. C. Meeker, "Fault tolerance of magnetic bearings by generalized bias current linearization," *IEEE Trans. Magn.*, vol. 31, no. 3, pp. 2304–2314, May 1995.

[15] D. Marquardt, "An algorithm for least-squares estimation of nonlinear parameters," *SIAM J. Appl. Math.*, vol. 11, pp. 431–441, 1963.

[16] D. C. Meeker, E. H. Maslen, and M. D. Noh, "An augmented circuit model for magnetic bearings including eddy currents, fringing, and leakage," *IEEE Trans. Magn.*, vol. 32, no. 4, pp. 3219–3227, Jul. 1996.

[17] H.-Y. Kim and C.-W. Lee, "Analysis of eddy-current loss for design of small active magnetic bearings with solid core and rotor," *IEEE Trans. Magn.*, vol. 40, no. 5, pp. 3293–3301, Sep. 2004.